Cytotoxicity in the age of nano: The role of fourth period transition metal oxide nanoparticle physicochemical properties

Charles C. Chusuei [a,*], Chi-Heng Wu [b], Shravan Mallavarapu [a], Fang Yao Stephen Hou [c], Chen-Ming Hsu [d], Jeffrey G. Winiarz [e], Robert S. Aronstam [b], Yue-Wern Huang [b,*]

[a] Department of Chemistry, Middle Tennessee State University, Box 390, 1301 East Main Street, Murfreesboro, TN 37132, USA
[b] Department of Biological Sciences, Missouri University of Science and Technology, 105 Schrenk Hall, 400 W. 11th Street, Rolla, MO 65409, USA
[c] Department of Clinical Laboratory Science, College of Health Sciences, Marquette University, P.O. Box 1881, Milwaukee, WI 53201, USA
[d] Department of Life Science, National Taiwan Normal University, 88 Ting-Chow Rd, Sec 4, Taipei 116, Taiwan, ROC
[e] Department of Chemistry, Missouri University of Science and Technology, 142 Schrenk Hall, 400 W. 11th Street, Rolla, MO 65409, USA

ARTICLE INFO

ABSTRACT

A clear understanding of physicochemical factors governing nanoparticle toxicity is still in its infancy. We used a systematic approach to delineate physicochemical properties of nanoparticles that govern cytotoxicity. The cytotoxicity of fourth period metal oxide nanoparticles (NPs): TiO_2, Cr_2O_3, Mn_2O_3, Fe_2O_3, NiO, CuO, and ZnO increases with the atomic number of the transition metal oxide. This trend was not cell-type specific, as observed in non-transformed human lung cells (BEAS-2B) and human bronchoalveolar carcinoma-derived cells (A549). Addition of NPs to the cell culture medium did not significantly alter pH. Physiochemical properties were assessed to discover the determinants of cytotoxicity: (1) point-of-zero charge (PZC) (i.e., isoelectric point) described the surface charge of NPs in cytosolic and lysosomal compartments; (2) relative number of available binding sites on the NP surface quantified by X-ray photoelectron spectroscopy was used to estimate the probability of biomolecular interactions on the particle surface; (3) band-gap energy measurements to predict electron abstraction from NPs which might lead to oxidative stress and subsequent cell death; and (4) ion dissolution. Our results indicate that cytotoxicity is a function of particle surface charge, the relative number of available surface binding sites, and metal ion dissolution from NPs. These findings provide a physicochemical basis for both risk assessment and the design of safer nanomaterials.

© 2013 Published by Elsevier Ireland Ltd.

1. Introduction

There are currently more than 2800 nanoparticulate-based applications commercially available. It is estimated that by 2017, this field will represent a $48.9 billion market [1]. As engineered nanoparticles (NPs) currently occupy a significant portion of the market and are anticipated to proliferate commercially, there is an urgent need to study their potential impact on human health and the environment.

To date, there exists no epidemiological or clinical evidence demonstrating that inhalation of NPs leads to adverse health effects in humans [2]. However, toxicological studies using animal models and cell cultures suggest that NPs are more toxic and inflammogenic than larger particles of similar composition and of equal mass [3]. We have demonstrated intricate relationships between NPs, production of ROS and changes in intracellular Ca^{2+} concentrations $[Ca^{2+}]_{in}$. These studies suggest that NPs can trigger cell death by multiple pathways [4]. NPs increase $[Ca^{2+}]_{in}$. Moderation of this increase by nifedipine suggests that a portion of this increase reflects the influx of extracellular calcium. Membrane disruption (e.g., as indicated by lipid peroxidation and membrane depolarization) may also play a role in this influx [4,5]. NPs also disrupt store-operated calcium entry (SOCE) [6]. The increase in intracellular ROS may also have multiple sources. There exist synergistic relationships between intracellular $[Ca^{2+}]$ and OS as the increases in both can be reduced by an antioxidant. Finally, while $[Ca^{2+}]_{in}$ and ROS affect each other, they induce cell death by distinct pathways.

Structural defects on the NPs, which can act as electron-donor/acceptor groups, may alter the electronic configuration and contribute to the formation of reactive oxygen species (ROS) [7]. Particle dissolution has also been considered as a factor in NP-induced toxic responses [8,9]. Particle size and morphology are factors that also contribute to toxicity [10,11]. It remains unclear whether additional physicochemical properties of metal oxide

* Corresponding authors. Tel.: +1 615 898 2079; fax: +1 615 494 7693 (C.C. Chusuei). Tel.: +1 573 341 6589; fax: +1 573 341 4821 (Y.-W. Huang).
E-mail addresses: Charles.Chusuei@mtsu.edu (C.C. Chusuei), huangy@mst.edu (Y.-W. Huang).

NPs dictate the toxic responses. To elucidate these properties, we systematically examined an array of oxides of transition metals in the fourth period of the Periodic Table (Ti, Cr, Mn, Fe, Ni, Cu, Zn). These types of nanomaterials have been extensively used in catalysis [12], magnetocooling [13], optical and recording devices [14,15], purification of enzymes and other biological materials [16], water purification devices [17], magnetic field assisted radionuclide therapy [18], embolics [19–21], cosmetic and skin care products, and targeted drug delivery agents [22–27]. This series of NPs offers an opportunity to investigate the determinants of toxicity, which may lead to the design of safer nanomaterials. Toxicity can be investigated using *in vitro* and *in vivo* systems. Both systems provide different information for various scientific purposes and in many cases are complementary to each other. As there are numerous nanomaterials, it is improbable, though not impossible, to investigate each nanomaterials with *in vivo* systems. Therefore, *in vitro* systems provide an alternative to study nanotoxicity in that (1) it is cost efficient, (2) it provides information to prioritize animal testing, and (3) it informs computational toxicology in the context of quantitative structure–activity relationship (QSARS).

We hypothesize that toxicity is a function of multiple physicochemical properties of nanoparticles. We selected TiO_2, Cr_2O_3, Mn_2O_3, Fe_2O_3, NiO, CuO, and ZnO NPs from a single commercial source to minimize variability. In order to determine whether cytotoxic responses are cell-type specific, two human lung cells were studied. Cells were exposed to these NPs and cytotoxicity was measured. Isoelectric points (i.e., point-of-zero charge), number of available surface binding sites, and band-gap energies of the NPs were measured. The NPs were also subjected to kinetic experiments to determine the extent of metal ion dissolution. Our results indicate that certain physicochemical properties of metal oxide NPs strongly correlate with cytotoxicity.

2. Materials and methods

2.1. Nanoparticles, reagents, and instrumentation protocols

The nanoparticles, reagents, and instrumentation protocols used in the experiments are detailed in the Appendix A. Transmission electron microscopy (TEM), X-ray photoelectron spectroscopy (XPS), and band gap measurements were performed on the NPs. Characterizations of graphite furnace atomic absorption analysis (GFAA) and inductive coupled plasma-mass spectrometry (ICP–MS) of the aqueous solution supernatants exposed to the NPs. Correlations of observed physicochemical properties of the materials were correlated with cytotoxicity.

2.2. Cell culture and exposure of cells to NPs

Human bronchial epithelial cells (BEAS-2B) and human bronchoalveolar carcinoma-derived cells (A549) are *in vitro* models considered as ideal for both studying the prevention of human lung carcinoma development and nanotoxicity testing [28]. These cells were maintained using the same procedures described in our previous studies [4,5,29–31].

Cells were grown at 37 °C in a 5% CO_2 humidified environment. Upon reaching 85% confluence, the cells were seeded into 24 well plates and allowed to attach for 24 h. The cell densities used followed ATCC protocol recommendations, and were well within sensitivity and detection limits of the analytical instruments used. To reduce experimental variation and ensure accuracy, particles were dried in a desiccator before being weighed on an analytical balance. Particles were suspended in cell culture medium, vortexed vigorously, and then sonicated. A series of dilutions in cell culture medium were performed to achieve desired concentrations. The

suspensions were immediately applied to cells to minimize agglomeration. Cells without NPs and reagent blanks were used as controls in each experiment.

2.3. Cytotoxicity assay and apoptosis

At the end of cell exposure to NP suspensions, the medium was discarded and the sulforhodamine B assay was used to determine cell viability relative to the control group [31]. Briefly, the cells were fixed with cold 10% trichloroacetic acid (TCA) for 1 h at 4 °C. The TCA solution was then discarded and the cells were washed three times with distilled water, followed by complete drying. Sulforhodamine B (0.2% in 1% acetic acid) was added to stain the cells for 30 min at room temperature. The staining solution was discarded and the cells were washed with 1% acetic acid three times to eliminate excess dye. After complete drying, the dye was dissolved in cold 10 mM Tris buffer (pH = 10.5). Aliquots (100 μL) of dye solution were transferred onto a 96-well plate, and absorbance was measured at 550 nm using a microplate reader (FLOURstar, BMG Labtechnologies, Durham, NC, USA).

Apoptotic cells were stained with annexin V–FITC and 7-aminoactinomycin D (7-AAD) followed by quantification using a Beckman Coulter Cell Lab Quanta SC System. Morphological examination of apoptotic cells was performed using the same dyes and observed with an Olympus IX 51 epifluorescence microscope.

2.4. Statistical analysis

For toxicity studies, three independent experiments were conducted, using triplicates for each treatment group. Data are expressed as mean ± standard deviation. The relationship between cytotoxicity and the physicochemical properties of nanoparticles were analyzed with Spearman's Rank Correlation Analysis.

3. Results

3.1. Size, morphology, and specific surface area

The approximate physical sizes (APS) of the seven commercially available transition metal oxide NPs ranged from 16 ± 5 nm (NiO) to 82 ± 31 nm (Mn_2O_3) (Table 1). The morphology of NPs observed with TEM was needle-like (TiO_2), spherical (Mn_2O_3, Fe_2O_3), or nearly spherical (Cr_2O_3, NiO, CuO, ZnO) (Fig. A1). The specific surface area (SSA) of NPs ranged from 8.71 m^2/g (Mn_2O_3) to 178.95 m^2/g (TiO_2). While TiO_2, Fe_2O_3, and CuO had similar sizes, they possessed distinctly different specific surface areas. This could be due to variations in surface porosity and discrepancy in morphology.

3.2. Influence of pH in cell culture medium on cell viability

Cytotoxicity of NPs may simply reflect changes in pH over time. To evaluate this possibility, NPs were added to the cell culture medium and pH was measured at 0, 6, 12, 18, and 24 h. Immediately after adding NPs to cells in medium, the pH became slightly elevated compared to the control cell in medium only. The pH fluctuated briefly, and then stabilized, except for NiO, which increased the pH between 12 and 24 h. Very little change in pH was observed at low NP concentrations (Table A1). As concentrations of NPs increase, pH variations increased with all NPs. However, the extent of pH fluctuations was 0.29 ± 0.14 and 0.31 ± 0.03 units with and without NPs, respectively. Cell morphology and size in the groups with NPs were similar to those in the control groups.

Table 1
Measured specific surface area, approximate physical size, and morphology of nanoparticles.

	TiO$_2$	Cr$_2$O$_3$	Mn$_2$O$_3$	Fe$_2$O$_3$	NiO	CuO	ZnO
SSA (m^2/g)	178.95	11.41	8.71	31.44	70.86	9.02	44.61
APS (nm)	46 ± 20	63 ± 34	82 ± 31	48 ± 13	16 ± 5	47 ± 24	27 ± 13
Morphology	Needle-like	Nearly spherical	Spherical	Spherical	Nearly spherical	Nearly spherical	Nearly spherical

3.3. Cytotoxicity and apoptosis

Seven nanosized oxides of transition metals (Ti, Cr, Mn, Fe, Ni, Cu, Zn) from the fourth period of the Periodic Table of Elements were selected to test our hypothesis that certain physicochemical properties of NPs contribute to cytotoxicity in human cells. Two human lung cell lines, BEAS-2B and A549, were tested to determine whether cytotoxicity is cell-type specific.

A 24-h study of A549 cells exposed to NPs shows a trend of toxicity, as revealed by cell viability. As the atomic number of the transition metal increases within the fourth period, cytotoxicity increases (Fig. 1). The toxicity falls into three categories: (1) TiO$_2$, Cr$_2$O$_3$, and Fe$_2$O$_3$ have zero to minimal toxicity (close to 100% cell viability); (2) Mn$_2$O$_3$ and NiO show typical dose-dependent toxicity (∼40% cell viability); and (3) CuO and ZnO induce potent toxicity within a narrow dose range (≲20% cell viability). A similar trend of toxicity is observed with BEAS cells (data not shown),

albeit with slight variations. Notably, both CuO and ZnO cause toxicity with a steep concentration range. There is a good correlation between cytotoxicity and atomic number (ρ = 0.93, Fig. 2). Cytotoxicity is observed in the form of apoptosis and necrosis (Fig. 3A–B). The combined populations of early apoptotic cells and late apoptotic/early necrotic cells treated with the highest concentrations of CuO (20 µg/mL) and ZnO (28 µg/mL) are 71.8 ± 7.6% and 28.4 ± 11.7%, respectively. The combined populations of early apoptotic cells and late apoptotic/early necrotic cells of the rest of five NPs range from 2.2 ± 0.7% and 6.1 ± 0.7%. The degree of apoptosis/necrosis corresponds with severity of cytotoxicity.

3.4. Physicochemical properties and toxicity

We hypothesize that cytotoxicity is a function of particle (i) surface charge, (ii) available surface binding sites, and (iii) dissolution of metal ions from metal oxide NPs. The particle surface charge,
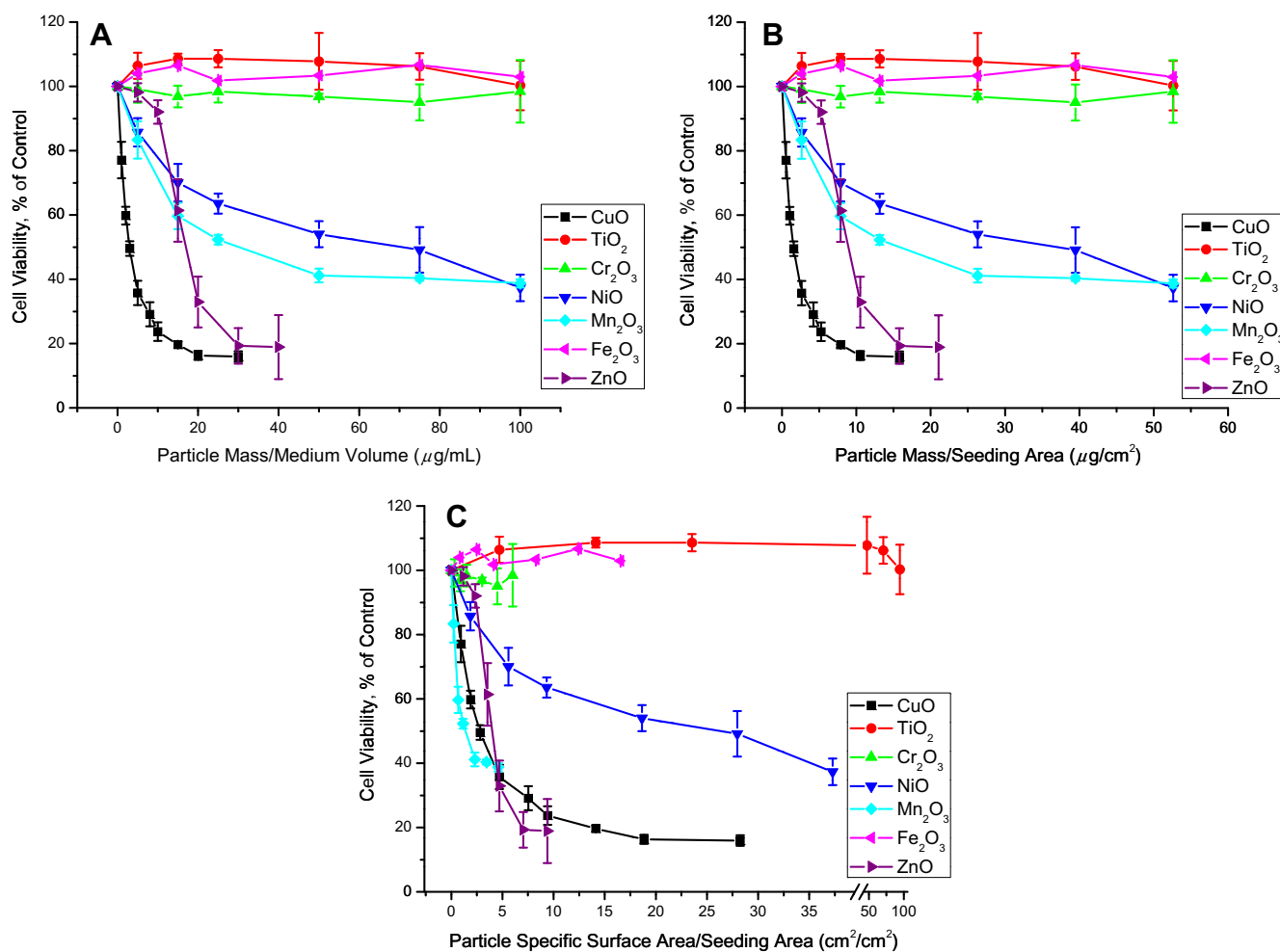

Fig. 1. Response of A549 cells to transition metal oxide nanoparticles based upon various dosimetry expressions: (A) particle mass/medium volume (µg/mL), (B) particle mass/seeding area (µg/cm^2), and (C) particle specific surface area/seeding area (cm^2/cm^2). Cell viability was determined by the sulforhoamine B method. Three independent experiments were conducted, using triplicates for each treatment group. Data are expressed as mean ± standard deviation.
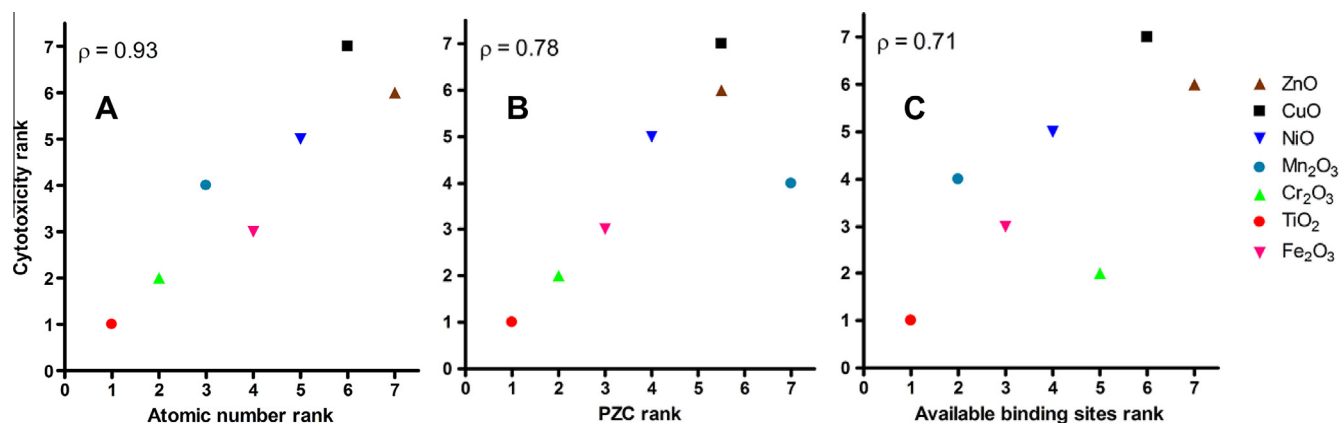
Fig. 2. (A) Spearman's Rank Correlation between cytotoxicity and atomic number of seven oxides of transition metals. As atomic number increases, cytotoxicity increases. The same trend occurs in both A549 and BEAS-2B cells. (B) Correlation between cytotoxicity of point-of-zero charge (PZC) of nanoparticles. Without the outlier Mn_2O_3, $\rho = 0.94$. (C) Correlation between cytotoxicity and available particle surface binding sites. Experiments were conducted at pH 7.4. Available surface binding sites were not estimated at pH 4.5 conditions. Acid etching effects observed in this pH region would skew quantitative measurements of physisorbed-to-metal oxide oxygen ratios.
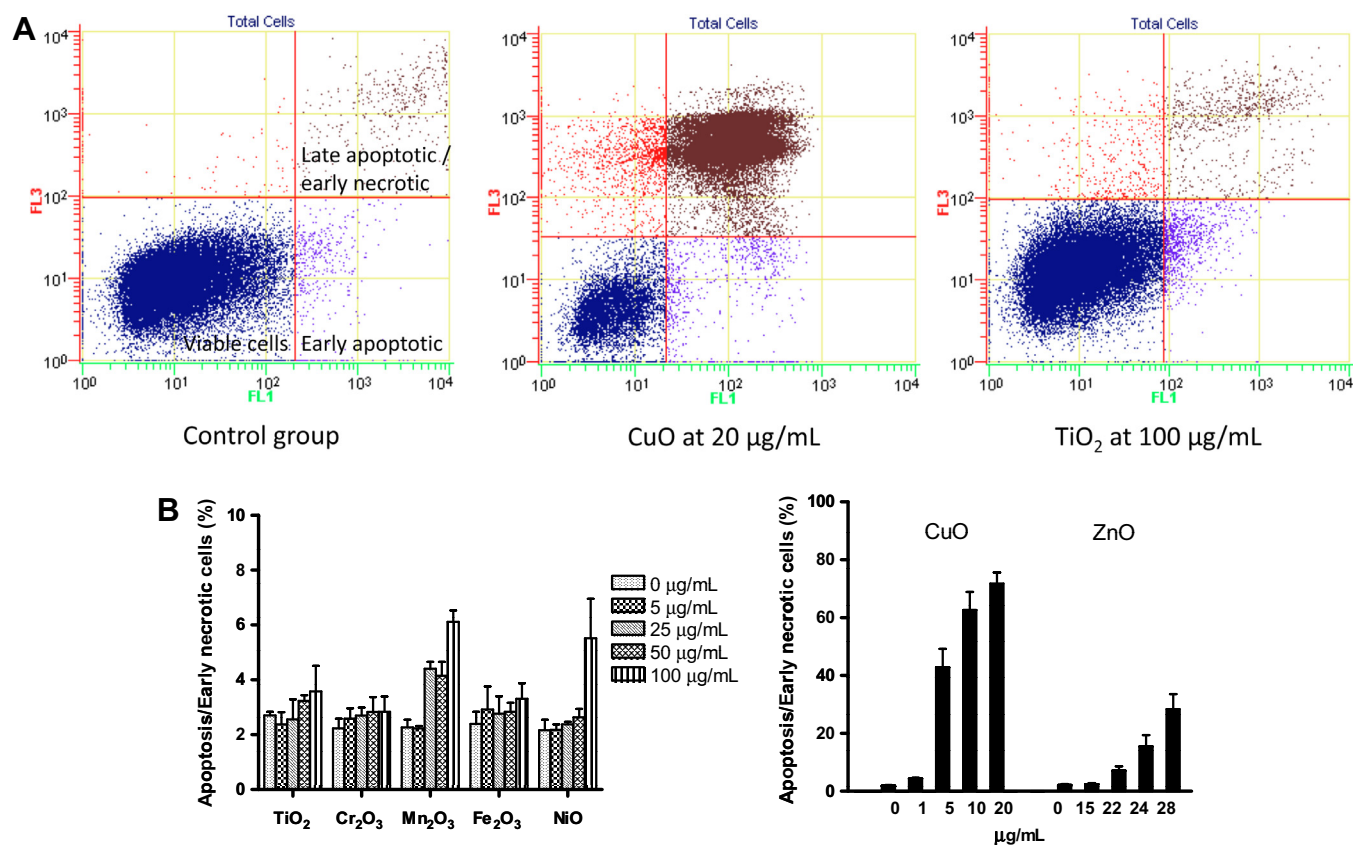

Fig. 3. Transition metal oxide nanoparticles induced cell death in A549 cells. Cells were treated with nanoparticles for 24 h followed by flow cytometric analysis using annexin V–FITC (AV, x-axis) and 7-aminoactinomycin D (7-AAD, y-axis): (A) AV positive/7-AAD negative (apoptotic) and AV-positive/7-AAD positive (late apoptosis, early necrosis); (B) Percentage of late apoptotic and early necrotic populations. Three independent experiments were conducted, using triplicates for each treatment group.

measured as PZCs, of the metal oxides are summarized in Fig. 4. Horizontal dashed lines within the PZC plot at pH = 4.5 and 7.4 denote the pH of the lysosomal and cytosolic environments, respectively. Noteworthy is the fact that as PZC increases, the cytotoxic effects of the NPs on the BEAS-2B and A549 cell lines increase, except for Mn_2O_3. Most of the PZC values cluster between 8 and 9, above both lysosomal and cytosolic environments, with the exception of TiO_2, which had a PZC of 6.9. Fig. 2B shows a good correlation between cytotoxicity and PZC calculated with Mn_2O_3 as an outlier ($\rho = 0.94$), and without Mn_2O_3 as an outlier ($\rho = 0.78$).

The relative number of available particle surface binding sites was measured by XPS (Table A2). A greater physisorbed-to-metal oxide oxygen ratio denotes more adsorption sites potentially available for cellular molecular binding. Fig. 5 shows a stack plot of XPS spectra of the O 1s orbitals of all NPs following a 16 h CC reaction at pH = 7.4. The chemical oxidation state denoting metal oxide (blue trace) is clearly defined for each respective nanoparticle. The XPS binding energies (BE) with full-width-at-half-maxima (fwhm) in parentheses were found to be at 530.0 (1.7), 529.6 (1.1), and 529.5 (1.4) eV, matching literature values for the metal oxide
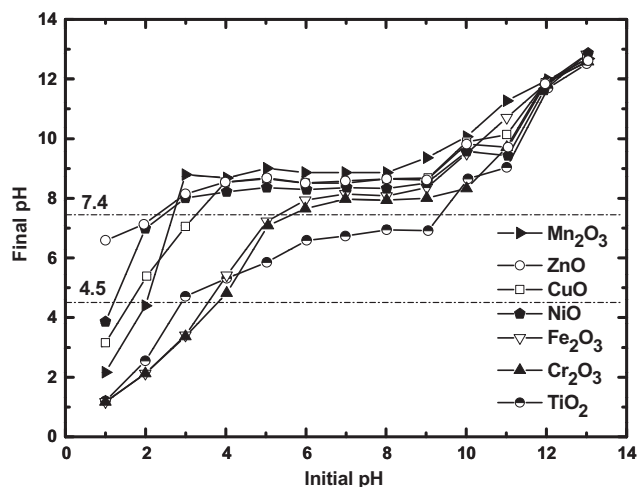
Fig. 4. Point-of-zero charge (PZC) initial pH versus final pH plots of Mn_2O_3, ZnO, CuO, NiO, Fe_2O_3, Cr_2O_3, and TiO_2 metal oxide nanoparticles. Horizontal lines at pH 7.4 and pH 4.5 denote cytosolic and lysosomal environments, respectively.
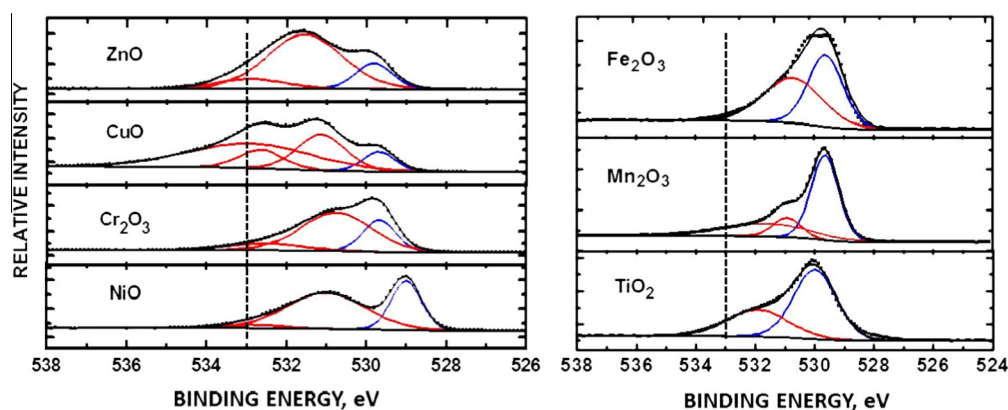
oxidation state for TiO_2 [32], Mn_2O_3 [33,34], and Fe_2O_3 [35,36], respectively. BEs observed at 531.9 (2.4) eV on TiO_2 [37–39], 530.9 (1.1) and 531.5 (4.0) eV on Mn_2O_3, and 529.5 (1.4) and 530.6 (2.4) eV on Fe_2O_3 are consistent with adsorbed hydroxyl species on these surfaces [40]. BEs of the metal oxide chemical state observed at O 1s = 529.0 (0.9), 529.7 (1.0), 529.7 (1.0) and 529.8 (1.1) eV, matched their literature values for NiO [41], Cr_2O_3 [42], CuO [43,44], and ZnO [45], respectively. BE peak centers at 531.0 (2.3) eV on NiO, 530.7 (2.1) and 532.5 (2.3) eV on Cr_2O_3, 531.1 (1.4) eV on CuO, and 531.6 (2.2) eV on ZnO are also consistent with the presence of adsorbed surface hydroxyls. The peak position at $\sim$531.5 eV could also emanate from adsorbed carbonyls (from atmospheric CO_2) [40]. The vertical dashed line (Fig. 5) denotes the BE chemical shift for the H_2O oxidation state. The O 1s BE peak centers at 532.9 (1.7) eV on NiO, 532.5 (2.3) eV on Cr_2O_3, 532.6 (1.3) and 532.9 (3.7) eV on CuO, and 532.9 (2.0) eV on ZnO denote adsorbed H_2O on these surfaces [39,40]. There was a good correlation between cytotoxicity and available nanoparticle surface binding sites ($\rho = 0.71$, Fig. 2C). According to these data, the relative number of available binding sites (Table A3) for each oxide is in

Fig. 5. XPS of O 1s orbitals of Fe_2O_3, Mn_2O_3, and TiO_2 metal oxide nanoparticles. XP spectra were deconvoluted using a 70:30 Gaussian–Lorenztian lineshape and applying Shirley background subtractions. Blue envelopes denote the metal oxide chemical oxidation state. Red envelopes denote adsorbed non-metal oxide oxygen. Vertical dashed lines denote the BE position for adsorbed H_2O. (For interpretation of the references to colour in this figure legend, the reader is referred to the web version of this article.)
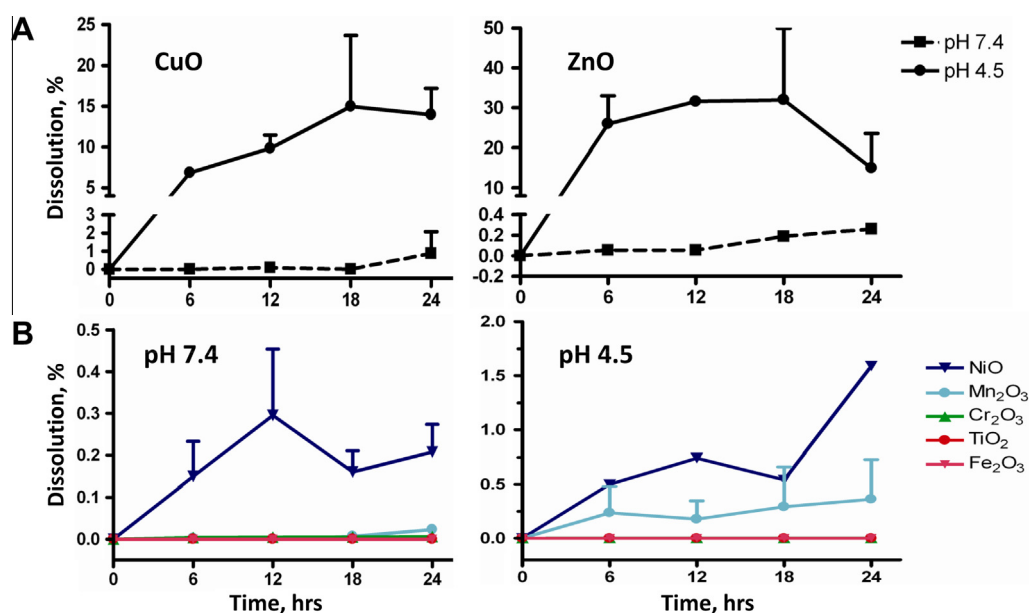

Fig. 6. ICP–MS and GFAA data from supernatants extracted from constant composition (CC) experiments of solutions in contact with metal oxide nanoparticles at pH 4.5 and pH 7.4, showing: (A) metal dissolution kinetics of CuO and ZnO nanoparticles and (B) metal dissolution kinetics of TiO_2, Cr_2O_3, Mn_2O_3, Fe_2O_3, and NiO nanoparticles. ICP–MS analysis was performed to analyze ions of Cu, Zn, Ti, Cr, Mn, and Ni in solution. GFAA analysis was performed to quantify the amount of ions of Fe in solution. $N = 3–6$. Data were expressed as mean ± standard deviation.
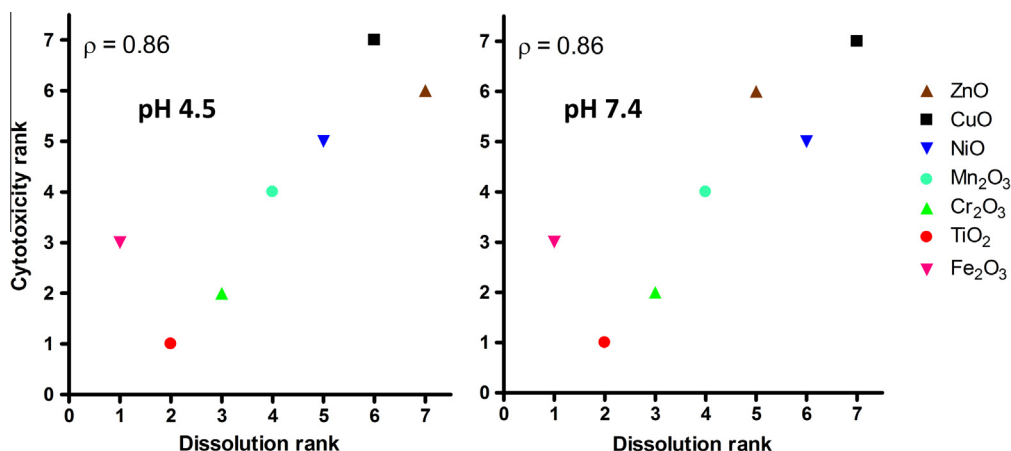
Fig. 7. Spearman's rank correlation between cytotoxicity and metal dissolution from nanoparticles.

Table 2
Correlation between cytotoxicity and physicochemical characteristics of transition metal oxide nanoparticles.

Dependent variable	Independent variable	Spearman's rank (ρ)
Cytotoxicity	Atomic number	0.93
	PZC	0.78
	# Of available binding sites	0.71
	Dissolution (at pH 7.4)	0.89
	Dissolution (at pH 4.5)	0.86

the following ascending order: TiO_2, Mn_2O_3, Fe_2O_3, NiO, Cr_2O_3, CuO, ZnO. With the exception of Cr_2O_3, the relative number of available binding sites correlated well with increased cytotoxicity and periodicity of the transition metal.

The dissolution kinetics of metals from metal oxide NPs over a period of 24 h was determined using CC experiments, followed by centrifugation and membrane dialysis. The samples were subjected to ICP–MS and GFAA analyses. Metal dissolution of CuO and ZnO NPs was prominent at acidic conditions (pH = 4.5). Increasing dissolution over a period of 18 h was observed with both NPs (Fig. 6A). Dissolution of CuO and ZnO NPs reached $14.97 \pm 6.16\%$ and $31.99 \pm 12.72\%$, respectively. Unexpectedly, there was a drop in ZnO dissolution between 18 and 24 h. At pH = 7.4, the highest dissolution of CuO and ZnO NPs was $0.87 \pm 0.85\%$ and $0.58 \pm 0.40\%$, respectively. Fig. 6B shows the dissolution kinetics of TiO, Cr_2O_3, Mn_2O_3, Fe_2O_3, and NiO NPs. Dissolution of NiO and Mn_2O_3 at pH = 4.5 and NiO at pH = 7.4 is the highest among them. TiO_2 and Cr_2O_3 at both pH conditions are considered undissolvable ($<< 0.006\%$). There was a good correlation between cytotoxicity and metal dissolution at both pH conditions ($\rho = 0.86$, Fig. 7). Table 2 summarizes the correlations found in our study between the physicochemical property and cytotoxicity as measured by Spearman's rank.

4. Discussion

We observe a clear trend in cytotoxicity: as the atomic number of transition metal oxide nanoparticles increases, cytotoxicity increases. This phenomenon is not cell-type specific as it occurs in both A549 and BEAS-2B cells. The response to NP exposure based upon particle mass dosimetry can be categorized into three toxicity groups: none to minimal (TiO_2, Cr_2O_3, Fe_2O_3), moderate dose-dependent (Mn_2O_3, NiO), and strong and steep (CuO, ZnO). The highest concentration tested was 100 g/mL; above which cells become engulfed by NPs. It remains unclear how this physical engulfment influences cellular response and survivorship, further complicating explanation for cytotoxicity.

The cell population reflects both cell proliferation and death. Thus, the reduced cell numbers observed in response to NPs could reflect reduced proliferation and/or increased cytotoxicity. Whether NPs tested in this study cause reduced proliferation was not addressed. Flow cytometric analysis revealed increased cell death. Both apoptotic cells and necrotic cells were observed. Microscopic examination (data not shown) revealed cells at different stages of dying: apoptotic budding, pre-necrotic apoptosis, apoptotic budding, apoptotic bodies, apoptotic shrink, and primary necrosis. The use of annexin V–FITC and 7-aminoactinomycin D (7-AAD) could not distinguish between cell death involving primary necrosis and apoptotic secondary necrosis; additional cellular biomarkers are needed in future studies to distinguish these processes.

Cytotoxicity of the metal oxide NPs in both cell lines correlates with their respective PZCs measured in water. Noteworthy is the fact that TiO_2 has a PZC of 6.9 while the pH of cell medium (with presence of cells) is 7.4, similar to that of the cytosol. The lowered PZC of the TiO_2 NPs indicates that they would be populated with negatively charged species due to Coulombic attractions, leading to low cellular uptake that requires crossing a negatively-charged cytoplasmic membrane. The explanation of lower bioavailability is limited by the fact that NPs could be coated by proteins in cell culture medium to form protein corona which may influence surface charge.

As size decreases, the total particle surface areas increase exponentially. The surface provides potential sites for interaction with biomolecules such as lipids, DNA, RNA, and protein. Using XPS to estimate the relative number of available particle surface binding sites, we attribute the changes in the O 1s line shapes (not emanating from the metal oxide oxidation state) to weakly adsorbed O-containing moieties at the metal oxide NP surface. The adsorbates are predominantly H_2O and hydroxyl groups; however, carbonates, CO, and CO_2 from atmosphere could also adsorb to the surface, and their binding energies (BEs) typically overlap with observed chemical shifts for adsorbed hydroxyls in the ~531 eV region [40]. Variations in the number of available surface sites can be attributed to the atomic level structures of the lattice oxygens within each oxide [46]. A periodic trend of increasing adsorbed-to-metal oxide oxygen is observed for the series of metal oxides studied, with the exception of Cr_2O_3, which deviates in that it has a pronounced amount of adsorbed oxygen, probably an artifact of CO_2 from solution exposure to the atmosphere. CO_2 has a propensity to adsorb onto Cr_2O_3. The relative large XPS intensity at O 1s BE at 531.2 eV (Fig. 5) has also been reported to emanate from a mixed

complex of $Cr_2O_3 \cdot nH_2O \cdot xCO_2$ formed from adsorbed atmospheric CO_2 into the aqueous solution [47]. The most toxic of nanoparticles analyzed in this series also has the highest adsorbed H_2O content; the vertical, dashed line denotes the chemical oxidation state for adsorbed H_2O, ZnO, and CuO have the highest PZCs and hence greatest degree of "protonation" via adsorption of hydronium ions (H_3O^+). Under aqueous solution physiological conditions, the metal oxide surface would be populated by excess H_3O^+, in accordance with Gouy–Chapman theory. During adsorption, the adsorbate would be electrically neutralized resulting in the observed, enhanced intensity denoting chemisorbed H_2O at 532.9 eV on the CuO and ZnO surfaces. Adsorbed H_2O is not pronounced on the Cr_2O_3, Mn_2O_3, Fe_2O_3, and NiO NP surfaces. Lesser absorption is observed with TiO_2 (Fig. 5), which has the lowest PZC in the series (below that of physiological pH), appearing at the leading edge of the BE envelope indicative of adsorbed hydroxyls at ~532 eV.

Dissolution of metals from metal oxides correlate with observed cytotoxicity. Dissolution kinetics of metals from metal oxide NPs suggests a significant release of Cu^{2+} and Zn^{2+} from CuO and ZnO oxides in acidic environment (pH = 4.5), but not neutral environment (pH = 7.4). A drop in metal dissolution of ZnO is observed between 18 and 24 h. We postulate that high concentrations of Zn^{2+} leads to re-absorption of the released ions onto the ZnO NPs. This action could result in an incomplete separation of ions from oxides during sample preparation. George et al. [48] also found significant Zn^{2+} dissolution from ZnO NPs in a 1000-min. kinetics study; equilibrium was not reached at the end of the experiment.

Metal dissolution of NiO at both pH = 4.5 and 7.4, and Mn_2O_3 at pH = 4.5 were lower than 1%, except for NiO at 24 h at pH = 4.5. Though the released Cu^{2+} and Zn^{2+} concentrations at the neutral environment are small, their potential effects may be significant, as these two ions are very toxic. Elevated levels of Zn^{2+} are toxic to a variety of cells, including PC-12, HeLa, and HT-29 cell lines, as well as primary cultures of cardiac myocytes and neurons [49]. Cu^{2+} increases cell death and impairs the colony-forming efficiency of human hepatoma cells [50]. Ni^{2+} released from nickel hydroxide nanoparticles plays a role of pulmonary toxicity in a whole-body inhalation study [51]. Additional studies have shown that exposure of particulate matter (PM)-associated ions, such as Cu^{2+} and Zn^{2+}, elevate oxidative stress and induce inflammatory responses [52–54]. Many NPs have been shown to use endocytosis as a major route for cellular entry [55,56]. Vesicles formed in endocytosis become early endosomes, late endosomes, and eventually acidic lysosomes. The time period that NPs remain in the acidic environment remains to be elucidated, as this factor would influence the degree of metal dissolution from the metal oxides. Experiments with soluble compounds such as $ZnSO_4$ and $CuCl_2$ can facilitate the understanding of the role of ions in nanotoxicity, with the limitation that kinetics of ions from these compounds differ from those released from transition metal oxides.

To summarize, we note the following trends correlating NP physicochemical properties with the cytotoxicity. As the atomic number of the transition metal increases, cytotoxicity increases. Cytotoxicity is not cell-type specific and does not reflect changes in pH or material band gap. Instead, cytotoxicity appears to predominantly be a function of (1) particle surface charge, (2) the number of available particle surface sites, and (3) metal ion dissolution from the NPs. Particle surface charge is pH dependent, and may thus influence the rate and routes of their cellular uptake as well as subsequent partitioning between organelles. The correlation of available surface binding sites with cytotoxicity increases the likelihood of NP interaction with biomolecules such as DNA, RNA, protein, and lipids. Dissolution of metals from oxides is pH dependent. Among the seven oxide NPs, release of Cu^{2+} and Zn^{2+} from their respective oxides is most likely to contribute to toxicity. Our observations show interplay of these three variables governing

cytotoxicity, and highlight this important consideration for risk assessment and design of safer nanomaterials.

Conflict of interest

None.

Acknowledgments

Appendix A. Supplementary data

Supplementary data associated with this article can be found, in the online version, at http://dx.doi.org/10.1016/j.cbi.2013.09.020.

References

[1] A. McWilliams, Nanotechnology: a realistic market assessment, NAN031E, BCC Research, 2012.
[2] NIOSH Current Intelligence Bulletin: Occupational Exposure to Titanium Dioxide, 2011-160, NIOSH, 2011.
[3] G. Oberdorster, E. Oberdorster, J. Oberdorster, Nanotoxicology: an emerging discipline evolving from studies of ultrafine particles, Environ. Health Perspect. 113 (2005) 823–839.
[4] C.C. Huang, R.S. Aronstam, D.R. Chen, Y.W. Huang, Oxidative stress, calcium homeostasis, and altered gene expression in human lung epithelial cells exposed to ZnO nanoparticles, Toxicol. In Vitro 24 (2010) 45–55.
[5] W. Lin, I. Stayton, Y.-W. Huang, X.-D. Zhou, Y. Ma, Cytotoxicity and cell membrane depolarization induced by aluminum oxide nanoparticles in human lung epithelial cells A549, Toxicol. Environ. Chem. 90 (2008) 983–996.
[6] H.J. Wang, A.C. Growcock, T.H. Tang, J. O'Hara, Y.-W. Huang, R.S. Aronstam, Zinc oxide nanoparticle disruption of store-operated calcium entry in a muscarinic receptor signaling pathway, Toxicol. In Vitro 24 (2010) 1953–1961.
[7] J. Jiang, G. Oberdorster, A. Elder, R. Gelein, P. Mercer, P. Biswas, Does nanoparticle activity depend upon size and crystal phase?, Nanotoxicology 2 (2008) 33–42
[8] N.M. Franklin, N.J. Rogers, S.C. Apte, G.E. Batley, G.E. Gadd, P.S. Casey, Comparative toxicity of nanoparticulate ZnO, bulk ZnO, and ZnCl$_2$ to a freshwater microalga (Pseudokirchneriella subcapitata): the importance of particle solubility, Environ. Sci. Technol. 41 (2007) 8484–8490.
[9] T. Xia, Y. Zhao, T. Sager, S. George, S. Pokhrel, N. Li, D. Schoenfeld, H. Meng, S. Lin, X. Wang, M. Wang, Z. Ji, J.I. Zink, L. Madler, V. Castranova, S. Lin, A.E. Nel, Decreased dissolution of ZnO by iron doping yields nanoparticles with reduced toxicity in the rodent lung and zebrafish embryos, ACS Nano 5 (2011) 1223–1235.
[10] Y. Pan, S. Neuss, A. Leifert, M. Fischler, F. Wen, U. Simon, G. Schmid, W. Brandau, W. Jahnen-Dechent, Size-dependent cytotoxicity of gold nanoparticles, Small 3 (2007) 1941–1949.
[11] X. Peng, S. Palma, N.S. Fisher, S.S. Wong, Effect of morphology of ZnO nanostructures on their toxicity to marine algae, Aquat. Toxicol. 102 (2011) 186–196.
[12] F.B. Noronha, M. Schmal, C. Nicot, B. Moraweck, R. Frety, Characterization of graphite supported palladium–cobalt catalysts by temperature-programmed reduction and magnetic measurements, J. Catal. 168 (1997) 42–50.
[13] S. Roy, D. Das, D. Chakravorty, D.C. Agrawal, Magnetic-properties of glass–metal nanocomposites prepared by the sol–gel route and hot-pressing, J. Appl. Phys. 74 (1993) 4746–4749.
[14] G.A. Prinz, Magnetoelectronics, Science 283 (1999) 330.
[15] J.K. Vassiliou, V. Mehrotra, M.W. Russell, E.P. Giannelis, R.D. Mcmichael, R.D. Shull, R.F. Ziolo, Magnetic and optical-properties of gamma-Fe$_2$O$_3$ nanocrystals, J. Appl. Phys. 73 (1993) 5109–5116.
[16] S.S. Airapetyan, G.G. Balayan, A.G. Khachatryan, Synthesis and some characteristics of magnetic matrices for fixation of biologically active substances, Russ. J. Appl. Chem. 74 (2001) 519–521.
[17] S. Kobe, G. Drazic, P.J. McGuiness, J. Strazisar, The influence of the magnetic field on the crystallisation form of calcium carbonate and the testing of a magnetic water-treatment device, J. Magn. Magn. Mater. 236 (2001) 71–76.
[18] C. Gruttner, J. Teller, Preparation and characterization of magnetic nanoparticles for in vivo applications, in: U. Hafeli, W. Schutt, J. Teller (Eds.), Scientific and Clinical Applications of Magnetic Carriers, Plenum Publishing Corporation, New York, 1997, p. 53.
[19] M.A. Howard III, M.S. Grady, R.C. Ritter, G.T. Gillies, W.C. Broaddus, R.G. Dacey, Magnetic neurosurgery, in: gildenbert (Ed.), Stereotactic and Functional Neurosurgery, Karger Pulbisher, Basel, Switzerland, 1996, pp. 102–107.

[20] M.A. Howard III, B.A. Abkes, M.C. Ollendieck, M.D. Noh, R.C. Ritter, G.T. Gillies, Measurement of the force required to move a neurosurgical probe through *in vivo* human brain tissue, IEEE Trans. Biomed. Eng. 46 (1999) 891–894.

[21] M.S. Grady, M.A. Howard, R.G. Dacey, W. Blume, M. Lawson, P. Werp, R.C. Ritter, Experimental study of the magnetic stereotaxis system for catheter manipulation within the brain, J. Neurosurg. 93 (2000) 282–288.

[22] E. Comini, G. Faglia, G. Sberveglieri, Z. Pan, Z.L. Wang, Stable and highly sensitive gas sensors based on semiconducting oxide nanobelts, Appl. Phys. Lett. 81 (2002) 1869–1871.

[23] X.D. Bai, P.X. Gao, Z.L. Wang, E.G. Wang, Dual-mode mechanical resonance of individual ZnO nanobelts, Appl. Phys. Lett. 28 (2003) 4806–4808.

[24] G.G. Ramakrishna, H.N. Ghosh, Effect of particle size on the reactivity of quantum size ZnO nanoparticles and charge-transfer dynamics with adsorbed catechols, Langmuir 19 (2003) 3006–3012.

[25] S.Y. Bae, H.W. Seo, Vertically aligned sulfur-doped ZnO nanowires synthesized via chemical vapor deposition, J. Phys. Chem. 108 (2004) 5206–5210.

[26] Y. Ding, Z.L. Wang, Structure analysis of nanowires and nanobelts by transmission electron microscopy, J. Phys. Chem. 108 (2004) 12280–12291.

[27] B.L. Zhu, C.S. Xie, D.W. Zeng, W.L. Song, A.H. Wang, Investigation of gas sensitivity of Sb-doped ZnO nanoparticles, Mater. Chem. Phys. 89 (2005) 148–153.

[28] A.K. Prahalad, J. Inmon, L.A. Dailey, M.C. Madden, A.J. Ghio, J.E. Gallagher, Air pollution particles mediated oxidative DNA base damage in a cell free system and in human airway epithelial cells in relation to particulate metal content and bioreactivity, Chem. Res. Toxicol. 14 (2001) 879–887.

[29] W. Lin, Y.-W. Huang, X.-D. Zhou, Y. Ma, In vitro toxicity of silica nanoparticles in human lung cancer cells, Toxicol. Appl. Pharmacol. 217 (2006) 252–259.

[30] W. Lin, Y.-W. Huang, X.D. Zhou, Y. Ma, Toxicity of cerium oxide nanoparticles in human lung cancer cells, Int. J. Toxicol. 25 (2006) 451–457.

[31] W. Lin, Y. Xu, C.-C. Huang, Y. Ma, K.B. Shannon, D.-R. Chen, Y.-W. Huang, Toxicity of nano- and micro-sized ZnO particles in human lung epithelial cells, J. Nanopart. Res. 11 (2009) 25–39.

[32] C.C. Chusuei, D.W. Goodman, M.J. Van Stipdonk, D.R. Justes, K.H. Loh, Solid–liquid adsorption of calcium phosphate on TiO₂, Langmuir 15 (1999) 7355–7360.

[33] M. Oku, K. Hirokawa, X-ray photoelectron spectroscopy of manganese–oxygen systems, J. Electron Spectrosc. Relat. Phenom. 7 (1975) 465–473.

[34] B.R. Strohmeier, D.M. Hercules, Surface spectroscopic characterization of Mn/Al₂O₃ catalysts, J. Phys. Chem. 88 (1984) 4922–4929.

[35] J. Haber, J. Stoch, L. Ungier, X-ray photoelectron spectra of oxygen in oxides of cobalt, nickel, iron, and zinc, J. Electron Spectrosc. Relat. Phenom. 9 (1976) 459–467.

[36] N.S. McIntyre, D.G. Zetaruk, X-ray photoelectron spectroscopic studies of iron oxides, Anal. Chem. 49 (1977) 1521–1529.

[37] D. Gonbeau, C. Guuimon, G. Pfister-Guillouzo, A. Levasseur, G. Meunier, R. Dormoy, XPS study of thin films of titanium oxysulfides, Surface Sci. 254 (1991) 81–89.

[38] W.E. Slinkard, P.B. DeGroot, Vanadium–titanium oxide catalysts for oxidation of butene to acetic acid, J. Catal. 68 (1981) 423–432.

[39] C.D. Wagner, D.A. Zatko, R.H. Raymond, Use of the oxygen KLL Auger lines in identification of surface chemical states by electron spectroscopy for chemical analysis, Anal. Chem. 52 (1980) 1445–1451.

[40] C.D. Wagner, W.M. Riggs, L.E. Davis, J.F. Moulder, G.E. Muilenbuerg, Handbook of X-ray Photoelectron Spectroscopy, Perkin–Elmer Corporation, Minnesota, 1979. p. 190.

[41] E.E. Khawaja, M.A. Salim, M.A. Khan, F.F. Al-del, G.D. Khatak, Z. Hussain, XPS, Auger, electrical and optical studies of vanadium phosphate glasses doped with nickel oxide, J. Non-Cryst. Solids 110 (1989) 33–43.

[42] W.-Y. Howng, R.J. Thorn, Investigation of the electronic structure of magnesium- and strontium-doped lanthanum chromite, chromia, and lanthana by X-ray photoelectron spectroscopy, J. Phys. Chem. Solids 41 (1980) 75–81.

[43] G. Ertl, R. Hierl, H. Knozinger, N. Thiele, H.P. Urbach, XPS study of copper aluminate catalysts, Appl. Surf. Sci. 5 (1980) 49–64.

[44] J.C. Otamiri, S.L.T. Andersson, A. Andersson, Ammoxidation of toluene by YBa₂Cu₃O₆+x and copper oxides: activity and XPS studies, Appl. Catal. 65 (1990) 159–174.

[45] B.R. Strohmeier, D.M. Hercules, Surface spectroscopic characterization of the interaction between zinc ions and γ-alumina, J. Catal. 86 (1984) 266–279.

[46] V.E. Henrich, P.A. Cox, The Surface Science of Metal Oxides, Cambridge University Press, New York, 1994. p. 464.

[47] D.L. Perry, L. Tsao, J.A. Taylor, The galena/dichromate solution interaction and the nature of the resulting chromium (III) species, Inorg. Chim. Acta 85 (1984) L57–L60.

[48] S. George, S. Pokhrel, T. Xia, B. Gilbert, Z. Ji, M. Schowalter, A. Rosenauer, R. Damoiseaux, K.A. Bradley, L. Madler, A.E. Nel, Use of a rapid cytotoxicity screening approach to engineer a safer zinc oxide nanoparticle through iron doping, ACS Nano 4 (2010) 15–29.

[49] R.A. Bozym, F. Chimienti, L.J. Giblin, G.W. Gross, I. Korichneva, Y. Li, S. Libert, W. Maret, M. Parviz, C.J. Frederickson, R.B. Thompson, Free zinc ions outside a narrow concentration range are toxic to a variety of cells in vitro, Exp. Biol. Med. (Maywood) 235 (2010) 741–750.

[50] N.S. Aston, N. Watt, I.E. Morton, M.S. Tanner, G.S. Evans, Copper toxicity affects proliferation and viability of human hepatoma cells (HepG2 line), Hum. Exp. Toxicol. 19 (2000) 367–376.

[51] G.S. Kang, P.A. Gillespie, A. Gunnison, H. Rengifo, J. Koberstein, L.C. Chen, Comparative pulmonary toxicity of inhaled nickel nanoparticles; role of deposited dose and solubility, Inhal. Toxicol. 23 (2011) 95–103.

[52] S. Becker, L.A. Dailey, J.M. Soukup, S.C. Grambow, R.B. Devlin, Y.-C. Huang, Seasonal variations in air pollution particle induced inflammatory mediator release and oxidative stress, Environ. Health Persp. 113 (2005) 1032–1038.

[53] S. Becker, J.M. Soukup, J.E. Gallagher, Differential particulate air pollution induced oxidant stress in human granulocytes, monocytes, and alveolar macrophages, Toxicol. In Vitro 16 (2002) 209–218.

[54] G.E. Hatch, E. Boykin, J.A. Graham, J. Lewtas, F. Pott, K. Loud, J.L. Mumford, Inhalable particles and pulmonary host defense: *in vivo* and *in vitro* effects of ambient air and combustion particles, Environ. Res. 36 (1985) 67–80.

[55] S.H. Wang, C.W. Lee, A. Chiou, P.K. Wei, Size-dependent endocytosis of gold nanoparticles studied by three-dimensional mapping of plasmonic scattering images, J. Nanobiotechnol. 8 (2010) 33.

[56] S. Zhang, J. Li, G. Lykotrafitis, G. Bao, S. Suresh, Size-dependent endocytosis of nanoparticles, Adv. Mater. 21 (2009) 419–424.